

# Hybridization of Persistent Homology with Neural Networks for Time-Series Prediction: A Case Study in Wave Height

Zixin Lin, Nur Fariha Syaquina Zulkepli\*, Mohd Shareduwan Mohd Kasihmuddin,  
R. U. Gobithaasan

**Address:** School of Mathematical Sciences, Universiti Sains Malaysia, 11800, Penang, Malaysia

**Email:** \*farihasyaqina@usm.my (N.F.S.Z)

## Abstract

Time-series prediction is an active area of research across various fields, often challenged by the fluctuating influence of short-term and long-term factors. In this study, we introduce a feature engineering method that enhances the predictive performance of neural network models. Specifically, we leverage computational topology techniques to derive valuable topological features from input data, boosting the predictive accuracy of our models. Our focus is on predicting wave heights, utilizing models based on topological features within feedforward neural networks (FNNs), recurrent neural networks (RNNs), long short-term memory networks (LSTM), and RNNs with gated recurrent units (GRU). For time-ahead predictions, the enhancements in  $R^2$  score were significant for FNNs, RNNs, LSTM, and GRU models. Additionally, these models also showed significant reductions in maximum errors and mean squared errors.

**Keywords:** Deep Learning, Computational Topology, Topological Data Analysis, Wave Height Prediction

## 1 Introduction

Utilizing neural networks to predict time series data presents considerable challenges, especially under conditions of abrupt environmental fluctuations. These challenges emanate from both the intrinsic characteristics of the data and the constraints inherent to neural network methodologies. A salient obstacle is the non-stationarity of environmental time series, in which key statistical properties—such as mean, variance, and autocorrelation—dynamically evolve, complicating predictive modeling [1]. Environmental data also typically exhibit significant variability and high noise levels, often resulting in models that overfit noise rather than extract the underlying patterns. Additionally, the temporal dependencies within environmental data are

complex, frequently nonlinear, non-periodic, and prone to abrupt changes, thereby increasing the difficulty of employing neural networks for predictive tasks [2].

Another significant limitation is the inadequacy of the available data, particularly the absence of comprehensive features, which substantially hampers model performance. This deficiency restricts the model’s capability to discern complex patterns, often leading to underfitting [3]. Comprehensive and representative features are essential for developing robust models that effectively generalize to novel, unseen datasets. A paucity of such features implies that the model may fail to account for all pivotal factors influencing the outcomes, thereby undermining generalization. Moreover, if the limited features utilized are not representative of the dataset’s diversity or the complexities of real-world scenarios, the resulting models can be biased. This, in turn, could perpetuate existing prejudices or overlook critical variables essential for accurate predictions.

In this study, we employ tools from topological data analysis (TDA) to engineer data features and enhance the predictive capabilities of models. TDA, an innovative domain within data science, draws on principles from topology—the study of properties invariant under continuous transformations. This approach excels at discerning the shape and structure of data, effectively revealing hidden patterns within complex, high-dimensional datasets. TDA methods demonstrate remarkable resilience to noise, prioritizing the identification of topologically significant features over mere artifacts of specific data sampling or measurement errors [4]. The proficiency of TDA in handling high-dimensional data spaces makes it particularly valuable in diverse fields such as genomics, image analysis, and complex networks [5]. Moreover, TDA offers strategies to address the curse of dimensionality, a pervasive issue that hampers many machine learning techniques in high-dimensional settings [6].

Persistent homology (PH) is a principal technique within TDA that explores multi-scale topological features of spaces [7]. This method probes how clusters, voids, tunnels, and other structural features appear and disappear as the scale of observation changes. Numerous studies highlight the successful application of PH in conjunction with learning models. For instance, Skaf and Laubenbacher (2022) demonstrated the utility of PH in decoding the intricate structure of biomedical data [8]. Obayashi et al., (2022) reviewed persistent homology’s application in materials research and its tools for data analysis [9]. Zulkepli et al., (2022) employed PH to analyze air quality data clustering, using topological distances to gauge dissimilarity between persistent diagrams [10]. Additional applications can be found in studies by Reani et al. [11], Munch [12], Pun et al. [13], and Townsend et al. [14].

In this study, we develop hybrid models combining persistent homology with neural networks (PHNN) to predict wave height data. Specifically, we create Feedforward Neural Networks (FNNs) and persistent homology-enhanced FNNs (PHFNNs) using a regression approach, focusing on models that take inputs and predict outputs within the same time step. This approach is inspired by the widespread use of FNNs in classical regression tasks. For instance, Talaat et al. (2020) [15] conducted load forecasting using multilayer FNNs with a regression

approach, while Amiri et al. (2023) [16] modeled wax deposition in crude oils using regression FNNs. See [17] for a comprehensive review. Additionally, we developed RNNs, LSTM, and GRU, along with their persistent homology-enhanced counterparts, for time-ahead prediction. Although the specific architecture designs of neural network models vary depending on the tasks or datasets they are applied to, their core objective is to learn a mapping—sometimes a stochastic one—to predict the unknown from the known.

Predicting wave heights is crucial for understanding the ocean’s role in global climate dynamics, monitoring marine ecosystem health, and improving navigational and disaster response strategies. Variations in wave height are key indicators of climate change, impacting coastal ecosystems and human settlements, and informing adaptive strategies in coastal management and infrastructure development [18]. Moreover, accurate wave height measurements and predictions are essential for maritime safety, optimizing shipping routes, and preparing responses to storm surges and tsunamis [19].

The structure of the paper is outlined as follows: Section 2 provides a discussion on the models and tools in TDA that are subsequently employed for analyzing and predicting wave height. Section 3 details the data, preprocessing methods, workflow processes, architectural designs of the neural network models, and presents a comparison of results. In Section 4, we delve into the contributions of our study, and discuss some limitations of our work. The paper concludes with Section 5.

## 2 Methodology

### 2.1 Feedforward Network

A feedforward neural networks (FNNs) [20] is a type of artificial neural network where connections between the nodes do not form a cycle. Data is fed into the network at the input layer and then propagated forward through the hidden layers to the output layer. In the  $i$ -th layer, the operation performed by each neuron can be represented as:

$$\mathbf{z}^{(i)} = f^{(i)} \left( \mathbf{h}^{(i-1)}; \mathbf{W}^{(i)}, b^{(i)} \right), \quad (1)$$

where  $\mathbf{z}^{(i)}$  represents the net input to the  $i$ -th layer,  $\mathbf{h}^{(i-1)}$  is the output from the previous layer,  $\mathbf{w}^{(i)}$  is the weight vector, and  $b^{(i)}$  is the bias term. The function  $f^{(i)}$  typically involves a dot product of the weights and inputs, plus the bias. The net input  $\mathbf{z}^{(i)}$  is then passed through an activation function  $\phi$  :

$$\mathbf{h}^{(i)} = \phi \left( \mathbf{z}^{(i)} \right), \quad (2)$$

where  $\mathbf{h}^{(i)}$  is the output of the neuron. The activation function introduces non-linearity into the network, enabling it to model complex relationships in the data. In this work, the operation  $f^{(i)}$

is defined as the affine transformation, given by

$$\mathbf{z}^{(i)} = \left(\mathbf{h}^{(i-1)}\right)^\top \mathbf{W}^{(i)} + b^{(i)}. \quad (3)$$

The activation function commonly used is the Rectified Linear Unit (ReLU), defined as:

$$\mathbf{h}^{(i)} = \text{ReLU}\left(\mathbf{z}^{(i)}\right) = \max\left(0, \mathbf{z}^{(i)}\right). \quad (4)$$

This ReLU activation function applies element-wise to the input  $\mathbf{z}^{(i)}$ , setting all negative values to zero and keeping all positive values unchanged. A simple FNNs is shown in Fig.1.

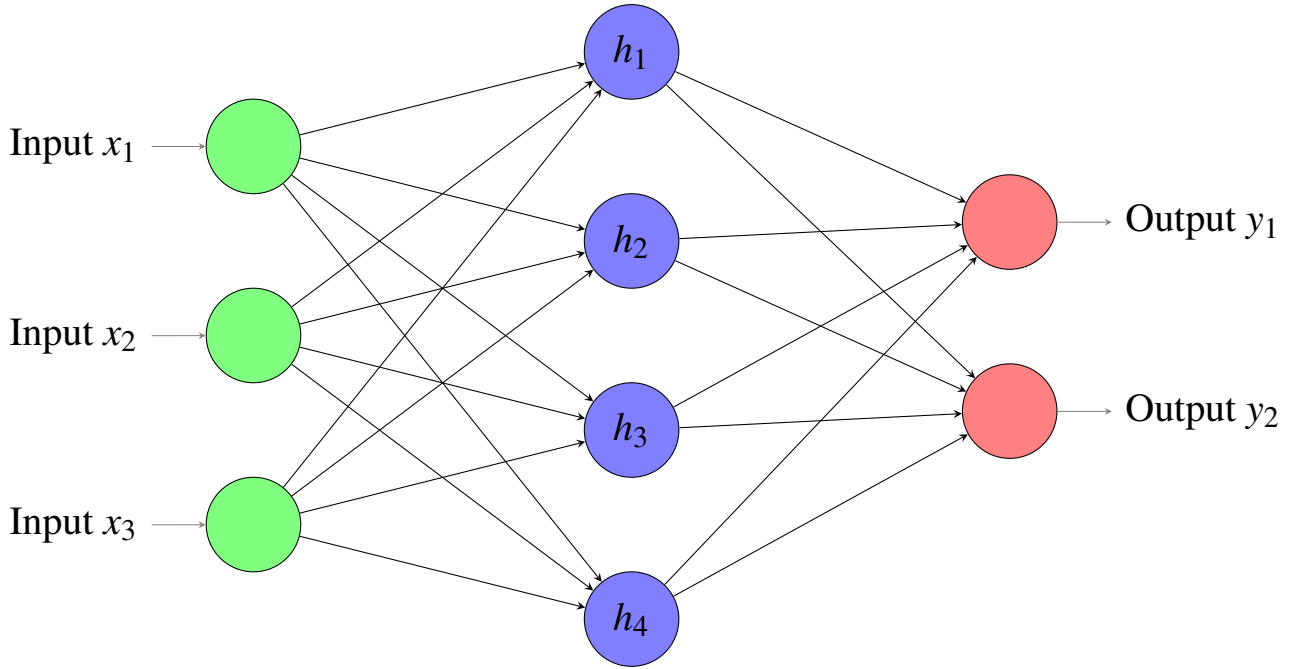


Figure 1: The figure illustrates a simple feedforward neural network comprising three layers: the input layer, the hidden layer, and the output layer. The input layer, represented by green circles, consists of 3 neurons. The hidden layer, depicted with blue circles, contains 4 neurons. The output layer, shown with red circles, consists of 2 neurons. Each layer is fully connected to the subsequent layer, indicating the flow of data through the network.

## 2.2 Recurrent Neural Network

Recurrent Neural Networks (RNNs) [21] learn the conditional distribution

$$\mathbb{P}\left(\mathbf{y}^{(T+t')} \mid \mathbf{x}^{(1)}, \dots, \mathbf{x}^{(T)}, \boldsymbol{\theta}\right), \quad (5)$$

where  $T$  and  $t'$  are non-negative integers. As shown in Fig.2, the hidden layers are updated by

$$\mathbf{h}^{(t)} = f\left(\mathbf{h}^{(t-1)}, \mathbf{x}^{(t)}; \boldsymbol{\theta}\right), \quad (6)$$

that takes the previous hidden state  $\mathbf{h}^{(t-1)}$  and the current input  $\mathbf{x}^{(t)}$ , along with the parameters  $\boldsymbol{\theta}$ , to compute the new hidden state  $\mathbf{h}^{(t)}$ . Usually, an activation function, such as ReLU, is applied to a linear combination of the previous hidden state  $\mathbf{h}^{(t-1)}$  and the current input  $\mathbf{x}^{(t)}$ , parameterized by the weight matrices  $\mathbf{W}$  and  $\mathbf{U}$ , and a bias term  $\mathbf{b}$ , shown as follows

$$\mathbf{h}^{(t)} = \text{ReLU}\left(\mathbf{b} + \mathbf{W}\mathbf{h}^{(t-1)} + \mathbf{U}\mathbf{x}^{(t)}\right). \quad (7)$$

This equation is a specific implementation of the function  $f$  in Eq.6, providing a non-linear transformation to capture complex patterns in the data.

The output  $\mathbf{o}^{(T)}$  at time step  $T$  is computed as a linear transformation of the hidden state  $\mathbf{h}^{(t)}$  using the weight matrix  $\mathbf{V}$  and a bias term  $\mathbf{c}$ . This output

$$\mathbf{o}^{(t)} = \mathbf{c} + \mathbf{V}\mathbf{h}^{(t)} \quad (8)$$

can be further processed to form the loss  $L^{(T)}$  for back-propagation steps.

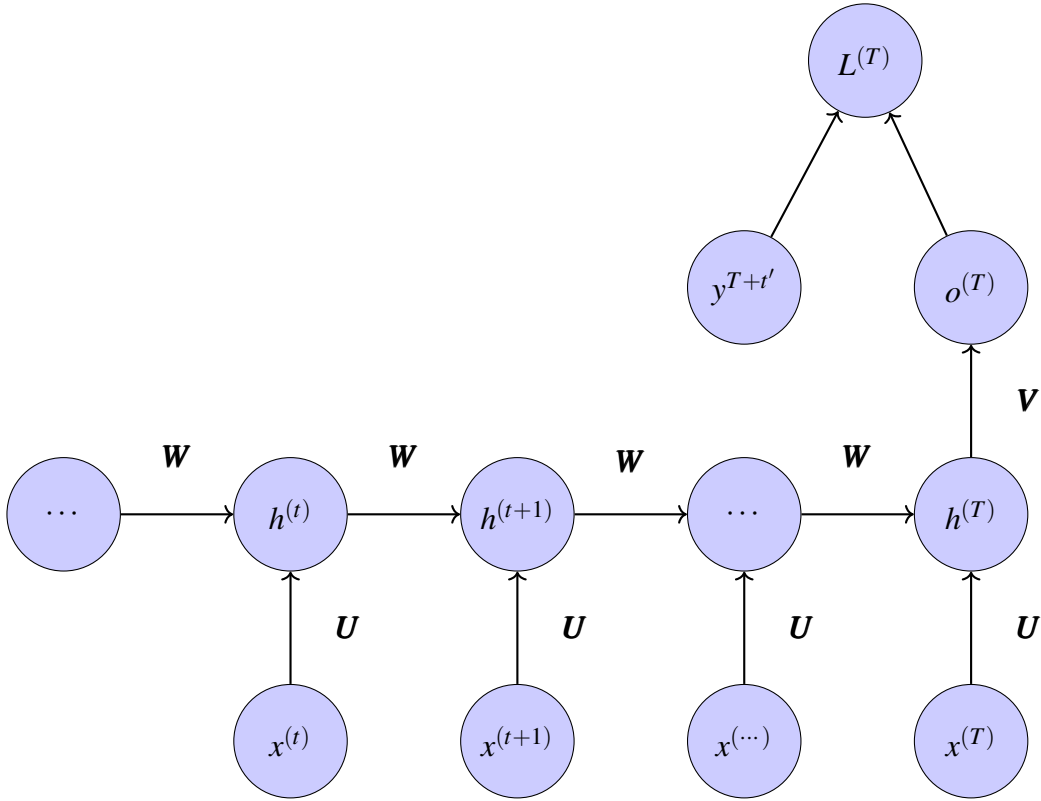


Figure 2: Schematic representation of a Recurrent Neural Network (RNN). The network processes input sequences  $x^{(t)}$  through a series of hidden states  $h^{(t)}$ , influenced by previous states and current inputs. Outputs  $o^{(T)}$  and observation  $y^{(T+t')}$  from  $t'$  time ahead are computed into the loss  $L^{(T)}$  for the subsequent back-propagation algorithm.

## 2.3 LSTM

Long Short-Term Memory (LSTM) [22] network is a specialized variant of RNN designed to address some of its limitations, particularly the problem of long-term dependencies. The key core of LSTM is the augment of state units before the update of hidden layers, and the updates are controlled by input gates, forget gates, and output gates. Specifically, the state  $\mathbf{s}^{(t)}$  is updated by

$$\mathbf{s}^{(t)} = \mathbf{f}^{(t)} \odot \mathbf{s}^{(t-1)} + \mathbf{g}^{(t)} \odot \sigma \left( \mathbf{b} + \mathbf{W}\mathbf{h}^{(t-1)} + \mathbf{U}\mathbf{x}^{(t)} \right), \quad (9)$$

where  $\sigma$  is the sigmoid function and  $\odot$  denotes the element-wise multiplication, while

$$\mathbf{f}^{(t)} = \sigma \left( \mathbf{b}^f + \mathbf{W}^f \mathbf{h}^{(t-1)} + \mathbf{U}^f \mathbf{x}^{(t)} \right) \quad (10)$$

denotes the forget gate and

$$\mathbf{g}^{(t)} = \sigma \left( \mathbf{b}^g + \mathbf{W}^g \mathbf{h}^{(t-1)} + \mathbf{U}^g \mathbf{x}^{(t)} \right) \quad (11)$$

denotes the input gate. Then  $\mathbf{h}^{(t)}$  is updated by

$$\mathbf{h}^{(t)} = \tanh \left( \mathbf{s}^{(t)} \right) \odot \mathbf{q}^{(t)}, \quad (12)$$

where

$$\mathbf{q}^{(t)} = \sigma \left( \mathbf{b}^o + \mathbf{W}^o \mathbf{h}^{(t-1)} + \mathbf{U}^o \mathbf{x}^{(t)} \right) \quad (13)$$

denotes the output gate.

## 2.4 GRU

In RNNs with gated recurrent unit (GRU) [23], the hidden layers are updated by:

$$\mathbf{h}^{(t)} = \mathbf{u}^{(t)} \odot \mathbf{h}^{(t-1)} + (1 - \mathbf{u}^{(t)}) \odot \tanh \left( \mathbf{b} + \mathbf{r}^{(t)} \odot \mathbf{W}\mathbf{h}^{(t-1)} + \mathbf{U}\mathbf{x}^{(t)} \right), \quad (14)$$

where

$$\mathbf{u}^{(t)} = \sigma \left( \mathbf{b}^u + \mathbf{W}^u \mathbf{h}^{(t-1)} + \mathbf{U}^u \mathbf{x}^{(t)} \right), \quad (15)$$

and

$$\mathbf{r}^{(t)} = \sigma \left( \mathbf{b}^r + \mathbf{W}^r \mathbf{h}^{(t-1)} + \mathbf{U}^r \mathbf{x}^{(t)} \right). \quad (16)$$

## 2.5 Taken's Embedding Theorem

Techniques from TDA usually analyze the topological structures of data in its phase space. There are numerous methods that can transform time-series to its phase space. One method to achieve this is by using forecast density and h-step-ahead predicted values to build a dissimi-

larity matrix that represents distances. However, this method requires assuming and defining a model for each time series under analysis, which can complicate the task. Another method commonly used in conjunction with the  $k$ -Nearest Neighbor method is dynamic time warping (DTW). However, this method is known to be sensitive to noise and is generally unsuitable for analyzing chaotic time-series data

As we delve deeper into the qualitative analysis of the series without depending on any predetermined models, we employ Takens' embedding theorem (the Quassi-attractor) to reconstruct time-series data in phase space. Given a time series  $\mathbf{X}^{(T)} = \{\mathbf{x}^{(t)}\}_{1 \leq t \leq T}$ , the phase space reconstruction is given by forming vectors  $P$  as follows:

$$P = \left\{ \left( \mathbf{x}^{(t)}, \mathbf{x}^{(t+\tau)}, \mathbf{x}^{(t+2\tau)}, \dots, \mathbf{x}^{(t+(d-1)\tau)} \right) \right\}_{1 \leq t \leq N-(d-1)\tau} \quad (17)$$

where  $\tau$  is the embedding time delay and  $d$  embedding dimension. Thus, a data point cloud  $P$  can be constructed from the time series  $\mathbf{X}^{(T)} = \{\mathbf{x}^{(t)}\}_{1 \leq t \leq T}$ .

## 2.6 Persistent Homology

Persistent homology is built on simplex and complex. A  $k$ -simplex denoted by  $\sigma_k$  is the convex hull formed by  $k + 1$  affinely independent points  $v_0, v_1, v_2, \dots, v_k$  as follows,

$$\sigma_k = \left\{ \lambda_0 v_0 + \lambda_1 v_1 + \dots + \lambda_k v_k \mid \sum_{i=0}^k \lambda_i = 1; 0 \leq \lambda_i \leq 1, i = 0, 1, \dots, k \right\}, \quad (18)$$

where  $\{v_i\}_{0 \leq i \leq k}$  are the vertices of the simplex. A simplicial complex denoted by  $K$  is a set of simplices that satisfies two conditions:

- Every face of a simplex in the complex is also in the complex (a face of a simplex is any simplex formed by a subset of its vertices).
- The intersection of any two simplices in the complex is either empty or a face of both simplices.

The dimension of a simplicial complex is defined as the largest dimension of any simplex within the complex. We present an example of a simplicial complex in Fig. 3.

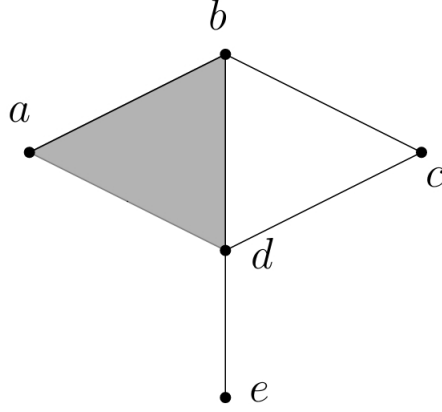


Figure 3: An illustration of a complex. Any vertex (e.g.,  $\{a\}$  or  $\{c\}$ ) is a 0-dimensional simplex. Any edge connecting two vertices (e.g.,  $\{a,b\}$ ) is a 1-dimensional simplex. The shaded triangle  $\{a,b,d\}$  represents a 2-dimensional simplex. Together, they form a 2-dimensional complex.

A filtration  $\mathcal{F} = \mathcal{F}(K)$  of a simplicial complex  $K$  is a nested sequence written with inclusion maps (continuous functions) as

$$\mathcal{F} : \emptyset = K_0 \hookrightarrow K_1 \hookrightarrow \dots \hookrightarrow K_n = K. \quad (19)$$

For the coefficients field from  $R$ -module  $\mathbb{Z}_{\mathbb{R}}$ . A  $p$ -chain is defined as

$$C_p = \{c_p \mid c_p = \sum_{i=1}^{m_p} \alpha_i \sigma_p^i, \alpha_i \in \mathbb{Z}_{\mathbb{R}}\}, \quad (20)$$

where  $m_p$  represents the number of  $p$ -simplices contained in  $K$ . When  $p < 0$  or  $p > n$ ,  $C_p = \emptyset$ . Given a  $p$ -simplex  $\sigma_p = \{v_0, \dots, v_p\}$ , the boundary operator  $\partial_p : C_p \rightarrow C_{p-1}$  is defined as  $\partial_p c_p = \sum_{i=1}^{m_p} \alpha_i (\partial_p \sigma_p^i)$  for a  $p$ -chain  $c_p = \sum_{i=1}^{m_p} \alpha_i \sigma_p^i \in C_p$ , where

$$\partial_p \sigma_p = \sum_{i=0}^p \{v_0, \dots, \hat{v}_i, \dots, v_p\} \quad (21)$$

and  $\hat{v}_i$  indicates that it is removed. Then the cycle group is defined as:

$$Z_p = \{c_p \mid c_p \in C_p, \partial_p c_p = 0\}, \quad (22)$$

and boundary group as:  $B_p = \{c_p \mid c_p \in C_p, \exists c_{p+1} \in C_{p+1} \text{ so that } \partial_{p+1} c_{p+1} = c_p\}$ , and homology group given by  $H_p = Z_p/B_p$  and its dimension is called the  $p$ -th Betti number [7].

Given a filtration of complex, a persistent homology is defined as:

$$0 = H_p(K_0) \rightarrow \dots \rightarrow H_p(K_i) \xrightarrow{h_p^{i,j}} H_p(K_j) \dots \rightarrow H_p(K). \quad (23)$$



where  $h_p^{i,j}$  denotes the inclusion map sending cycles in  $H_p(K_i)$  to  $H_p(K_j)$  for any  $0 \leq i \leq j \leq n$ .

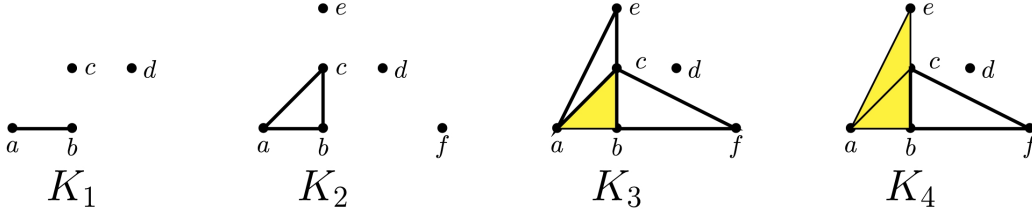


Figure 4: A nested sequence of complex.  $K_1 = \{\{a\}, \{b\}, \{c\}, \{d\}, \{a, b\}\}$  and  $K_1 \subseteq K_2$ , while  $K_3 = \{\{a\}, \{b\}, \{c\}, \{d\}, \{e\}, \{f\}, \{b, c\}, \{c, a\}, \{a, b\}, \{a, e\}, \{e, c\}, \{c, f\}, \{f, b\}, \{a, b, c\}\}$ . Obviously,  $K_4 = K_3 \cup \{a, c, e\}$ .

A complex filtration process effectively captures the dynamic contours of datasets by tracking the emergence and disappearance of holes or voids, specifically cycles that are not boundaries. For example, in  $K_2$  (Fig.4), the three 1-simplices  $\{a, b\}, \{b, c\}, \{c, a\}$  form a cycle. This cycle serves as the boundary for the simplex  $\{a, b, c\}$  in  $K_3$ . In  $K_2$ , these simplices do not form the boundary of any simplex, as  $\{a, b, c\}$  (yellow triangle in  $K_3$ ) does not exist in  $K_2$ . Thus, they create a non-boundary cycle in  $K_2$  that becomes a boundary in  $K_3$ . The hole defined by  $\{a, b\}, \{b, c\}, \{c, a\}$  is born at stage 2 and dies at stage 3.

A persistence diagram (PD) captures the birth and death of these holes within Persistent Homology (PH), represented as a set of 2D points  $\{(b_i, d_i)\}_{1 \leq i \leq N}$ . Here,  $N$  is the total number of holes, with  $b_i$  indicating birth and  $d_i$  indicating death. The birth-death pairs of the filtration shown in Fig. 4 are illustrated in Fig.5.

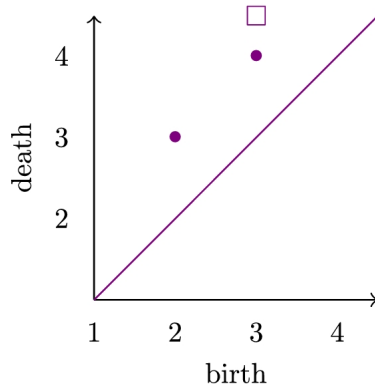


Figure 5: A persistent diagram for 1-dimensional voids of the complex filtration shown in Fig. 4. The figure is sourced from [24].

For a given data point cloud  $P$ , the Vietoris-Rips complex is defined as:

$$\text{VR}_\varepsilon(P) = \{\sigma \subseteq P \mid \text{diam}(\sigma) < 2\varepsilon\}. \quad (24)$$

This complex is the default type used in our work. The equation indicates that by varying the diameter parameter  $\varepsilon$ , we can obtain a nested sequence of simplicial complexes. This allows us to compute persistent homology, which captures the topological features of the data set across different scales.

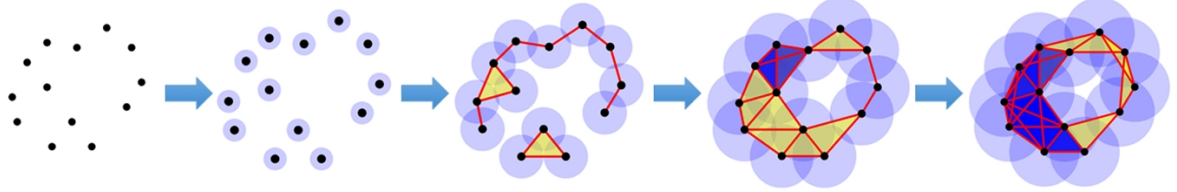


Figure 6: The illustration, sourced from [13], shows the filtration process in persistent homology of Vietoris-Rips complex. Each point is associated with an identically-sized sphere, and the sphere's radius is used as the filtration parameter. As the radius increases, a series of nested simplicial complexes and the persistent homology is generated.

Given a finite persistence diagram  $D = \{(b_i, d_i)\}_{i \in [1, n]}$ , the persistence landscape is defined as the function on  $D$ :

$$\lambda(k, t) := k\text{-th largest value of } [\min\{t - b_i, d_i - t\}]_+ \text{ for } i \in [1, N], \quad (25)$$

where  $[c]_+$  denotes  $\max\{c, 0\}$ . Fig.7 presents an illustrative example. Given a set of discrete values  $[t_1, t_2, \dots, t_{\ell-1}, t_{\ell}]$ , one can extract a scalar representing the topological features as follows:

$$\bar{\lambda}(k, t) = \frac{1}{k\ell} \sum_{H_p} \left( \sum_{i=1}^{\ell} \lambda_D^{H_p}(k, t_i) \right). \quad (26)$$

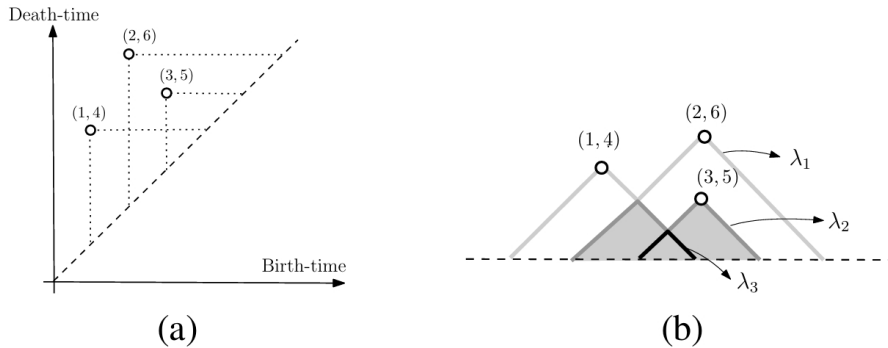


Figure 7: Sourced from [7] (a) A persistence diagram and its corresponding persistent landscape are in (b), where  $\lambda_k := \lambda(k, \cdot)$  for  $k = 1, 2$ , and 3.

## 2.7 An example of constructing topological representation

In this section, we present an example of transforming a time series into its topological representation. We select a dataset recorded by buoy station *c46208* and focus on the feature *VTPK* (more details are available in section 3.1). This feature contains one observation per hour, totaling 24 observations per day, spanning from January 1, 2016, to December 31, 2018. We plot the 24 observations from Oct. 21, 2016 (randomly selected), in the top figure of Fig.8. Then, using the embedding parameters: dimension  $m = 3$  and time delay  $\tau = 1$ , we reconstruct the top figure into its phase space representation, shown in the bottom figure of Fig.8.

Subsequently, we construct the Vietoris-Rips complex (Eq. 24) for the point cloud derived from the time series. We scale the diameter  $\varepsilon$  from  $0 \rightarrow \sup_{(x,y) \in P} \|x - y\|_2$ , where  $P$  is the data point cloud. We selected the dimensions  $p \in \{0, 1, 2\}$ , and constructed nested sequences of complexes in these three dimensions. From these, we extract the persistent homologies (PHs), as shown below:

$$0 = H_0(\text{VR}_0(P)) \rightarrow \cdots \rightarrow H_0(\text{VR}_{\varepsilon_i}(P)) \rightarrow \cdots \rightarrow H_0(\text{VR}_{\varepsilon_j}(P)) \cdots \rightarrow H_0(\text{VR}_{\varepsilon_n}(P)), \quad (27)$$

$$0 = H_1(\text{VR}_0(P)) \rightarrow \cdots \rightarrow H_1(\text{VR}_{\varepsilon_i}(P)) \rightarrow \cdots \rightarrow H_1(\text{VR}_{\varepsilon_j}(P)) \cdots \rightarrow H_1(\text{VR}_{\varepsilon_n}(P)), \quad (28)$$

and

$$0 = H_2(\text{VR}_0(P)) \rightarrow \cdots \rightarrow H_2(\text{VR}_{\varepsilon_i}(P)) \rightarrow \cdots \rightarrow H_2(\text{VR}_{\varepsilon_j}(P)) \cdots \rightarrow H_2(\text{VR}_{\varepsilon_n}(P)), \quad (29)$$

where  $\varepsilon_n = \sup_{(x,y) \in P} \|x - y\|_2$ . We extracted their persistence diagrams  $D = \{(b_i, d_i)\}$  and plotted them together in the right figure of Fig. 9.

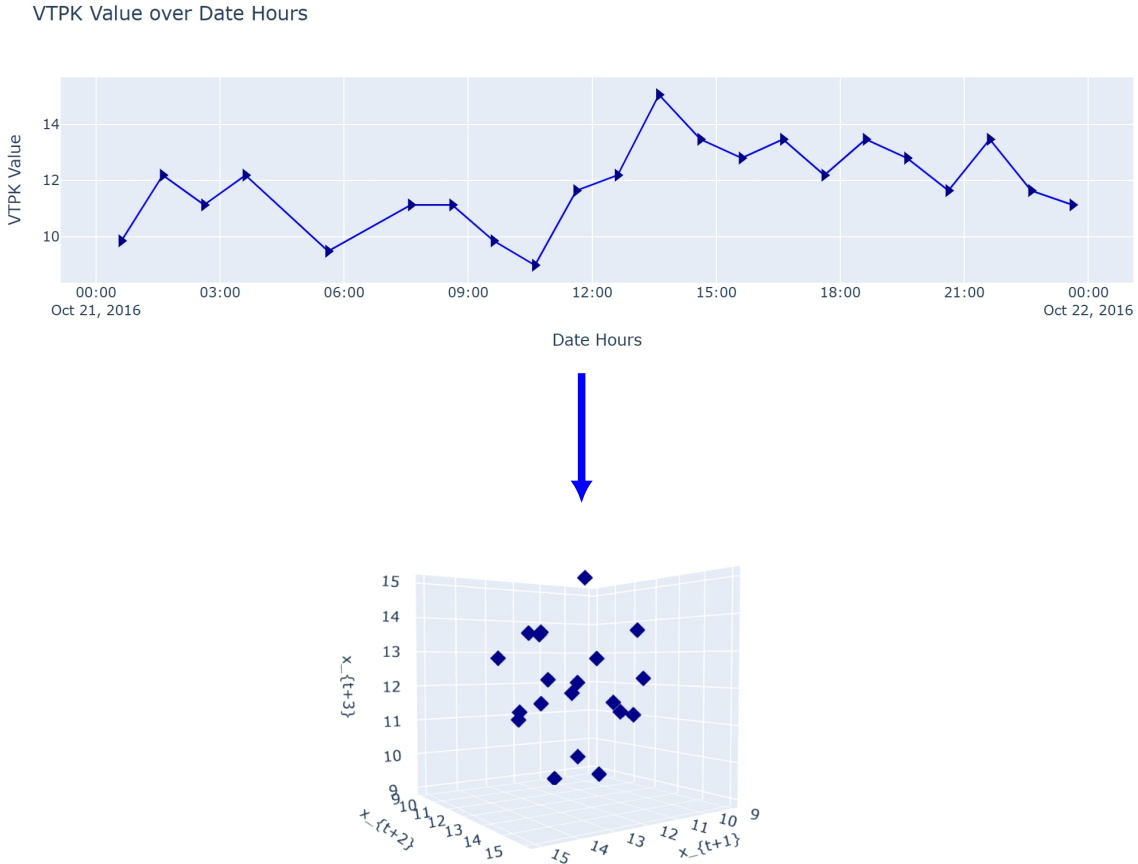


Figure 8: Transformation of a time series into its phase space representation. (Top) A time series containing observations of VTPK values over 24 hours on Oct.21, 2016. (Bottom) The phase space representation of the time series, constructed using the embedding theorem with  $m = 3$  and  $\tau = 1$ .

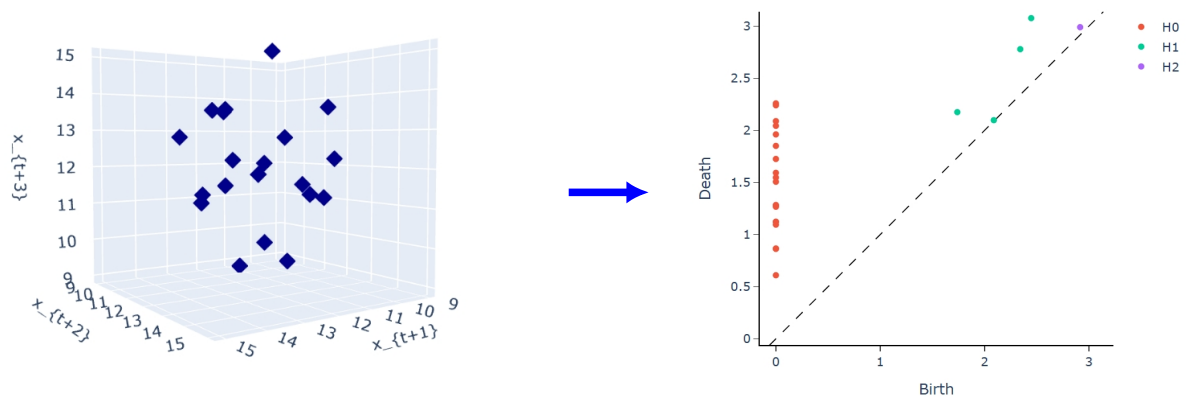


Figure 9: Transformation of point cloud data to its topological representation in the persistence diagram. (Left) The phase space representation of a time series, as shown in the top figure of Fig. 8. (Right) A persistence diagram, where  $H_0$  indicates the birth-death pairs of 0-dimensional homology circles (red dots),  $H_1$  indicates 1-dimensional homology circles (green dots), and  $H_2$  indicates 2-dimensional homology circles (purple dots).

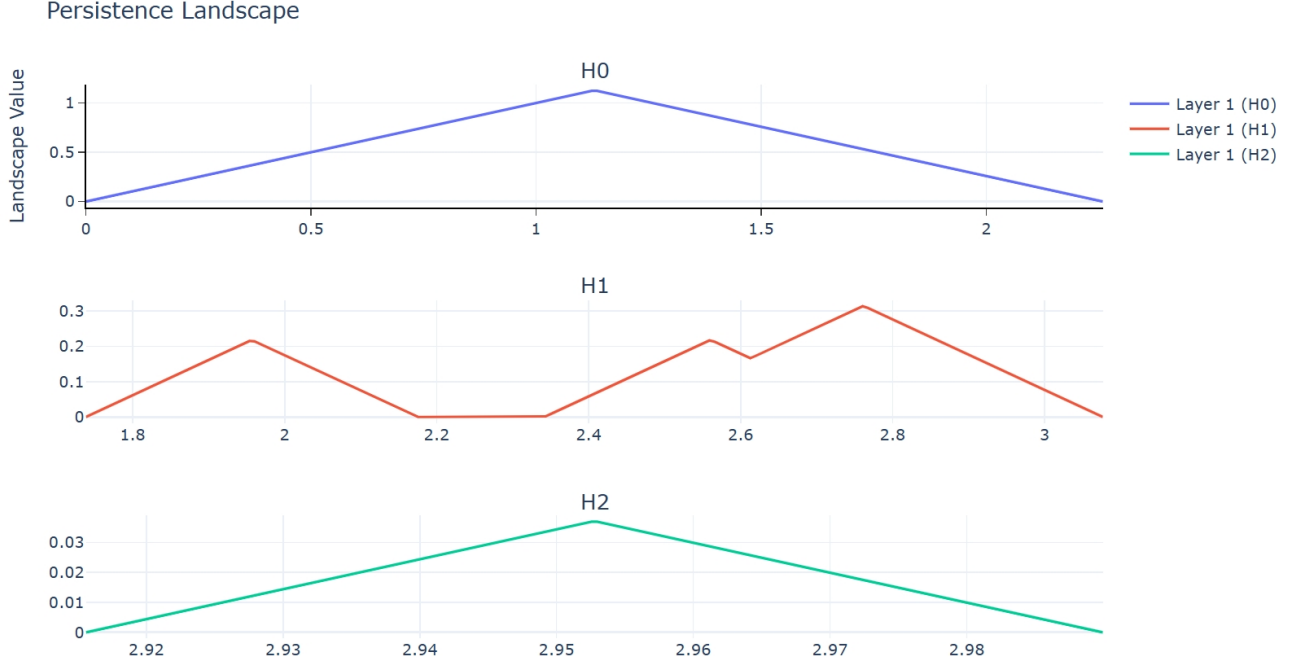


Figure 10: PL constructed from the right figure of Fig.9. (Top) The first layer PL for 0-dimensional persistent homology, colored blue. (Middle) The first layer PL for 1-dimensional persistent homology, colored red. (Bottom) The first layer PL for 2-dimensional persistent homology, colored green.

We then constructed the persistence landscape for the persistence diagram, as shown in Eq. 25. We selected  $k = 1$ , representing the largest value of  $[\min\{t - b_i, d_i - t\}]_+$ . The functions of the persistence landscape are plotted in Fig. 10, with different subfigures for the persistent homology of each dimension. We then employed the binning approach, discretizing the interval of each function into 200 values with equal gaps. We then extracted a scalar as follows:

$$\bar{\lambda} = \frac{1}{600} \sum_{H_p=0}^2 \left( \sum_{i=1}^{200} \lambda_D^{H_p}(1, t_i) \right). \quad (30)$$

This represents the topological characteristics of the time series observations over 24 hours on Oct.21 2016. Subsequently, we repeated the described process for all days from January 1, 2016, to December 31, 2018, using the data collected by buoy station c46208, and obtained their topological representations using Eq. 30.

We plotted the results in Fig.11. It is evident that we obtained a new time series of topological features for the time series of VTPK values. We can repeat the entire process for all the features we have, thereby doubling the number of features available for training network models.



Figure 11: A time series of VTPK's topological features. The y-axis represents the scalar values obtained from Eq.30, applied to all days from January 1, 2016, to December 31, 2018. The x-axis represents the time period.

### 3 Data, Analysis and Results

#### 3.1 Data and preprocessing

This section describes the dataset used in our study, which comprises data from a Canadian buoy station identified by the code c46208. The station has been collecting data influenced by the weather patterns of the Pacific Ocean. The dataset includes records of several variables from January 1, 2016, to December 31, 2018, as shown below:

- **VCAR**: Characteristic significant wave height (calculated by MEDS) (m)
- **VTPK**: Wave spectrum peak period (calculated by MEDS) (s)
- **WDIR**: Direction from which the wind is blowing ( $^{\circ}$  True)
- **GSPD**: Gust wind speed (m/s)
- **ATMS**: Atmospheric pressure at sea level (mbar)
- **DRYT**: Dry bulb temperature ( $^{\circ}$ C)
- **SSTP**: Sea surface temperature ( $^{\circ}$ C)

These parameters are denoted using the GF3 standard codes. A detailed explanation of the standard codes is available in the [Format Description](#). The data source is the Marine Environmental Data Service ([MEDS](#)). Each dataset from the station contains 24 observations (one observation of a seven-variable tuple containing the parameters listed above per hour) per day during the period. Thus, we have approximately 26,280 records ( $365 \times 24 \times 3$ ) for each parameter. In this work, our goal is to predict the daily mean VCAR one day ahead over an extended period of

about six months. As we will demonstrate in Section 3, Persistent-Homology networks provide a superior alternative for prediction. We show the location of the station in Fig.12, and the distributions of variables in Fig.13.

The data preprocessing includes several steps:

1. Normalization: The normalization process was performed using the formula:

$$\mathbf{x}_{\text{normalized}} = \frac{\mathbf{x} - \text{mean}(\mathbf{x})}{\text{std}(\mathbf{x})}, \quad (31)$$

where  $\text{mean}(\mathbf{x})$  is the mean of  $\mathbf{x}$  and  $\text{std}(\mathbf{x})$  is the standard deviation of  $\mathbf{x}$ .

2. Outlier handling: We adopted the  $z$ -score technique, removing data points where

$$|\mathbf{x}_{\text{normalized}}| > 3. \quad (32)$$

3. Missing data handling: For short periods of missing data (less than 5 days), we filled the data by averaging the previous week's data. For longer periods of missing data (5 days or more), we excluded the data.



Figure 12: A map showing the location of the buoy station. The location are indicated by the purple dot with blue code. The station is cloated in West Moresby with latitude 52.520N and longitude 132.690W. The water depth of the station is 2950m, and the anemometer height is 5m above the site elevation

### 3.2 Hyperparameters and working flow

In this section, we present the key hyperparameters selected for the architecture designs of network models. These hyperparameters are divided into three groups. The first group is `primary_para_grid` that contains a grid of hyperparameters over which we conducted a search to optimize model performance. Once we find the best parameters in this group for some models, we fixed them when training PH network models. The group contains the following hyperparameters

$$\{T_{\text{list}}, \{\mathbf{X}[i]\}_{i=1}^K\},$$

where  $T_{\text{list}}$  is a list of the lengths of sequence  $(\mathbf{x}^{(1)}, \dots, \mathbf{x}^{(T)})$  defined in Eq.5 over which we searched for the best performance in the validation process, and  $\{\mathbf{X}[i]\}_{i=1}^K$  is the set of all features in the data set.  $T_{\text{list}}$  is taken as

$$\{5 \times i \mid 1 \leq i \leq 6\}.$$

The second group is `secondary_para_grid`. This group includes

$$\{\text{num\_layers}, \text{lr}, \text{num\_hid}, \text{thresh}\}$$

These hyperparameters were determined through a cross-validation process. The following are a detailed explanation ( $i$  is an integer):

- `num_layers`: The number of hidden layers. We searched it over

$$\{1 \times i \mid 2 \leq i \leq 40\}.$$

- `lr`: The learning rate of the optimizer, we searched it over

$$\{5 \times 10^{-i} \mid 2 \leq i \leq 4\}.$$

- `num_hid`: The number of units in the hidden layers. We searched it over

$$\{3 \times i \mid 1 \leq i \leq 20\}.$$

- `thresh`: Threshold of stopping the training process when  $\text{loss} < \text{thresh}$ . We searched it over

$$\{10^{-2} \times 5 \times i \mid 1 \leq i \leq 4\}.$$

The third group is `fixed_para_grid` that contains hyperparameters whose values are kept fixed throughout the entire process. The details are as follows:

- $\tau$ : The time delay in the Embedding Technique, fixed as  $\tau = 1$ .



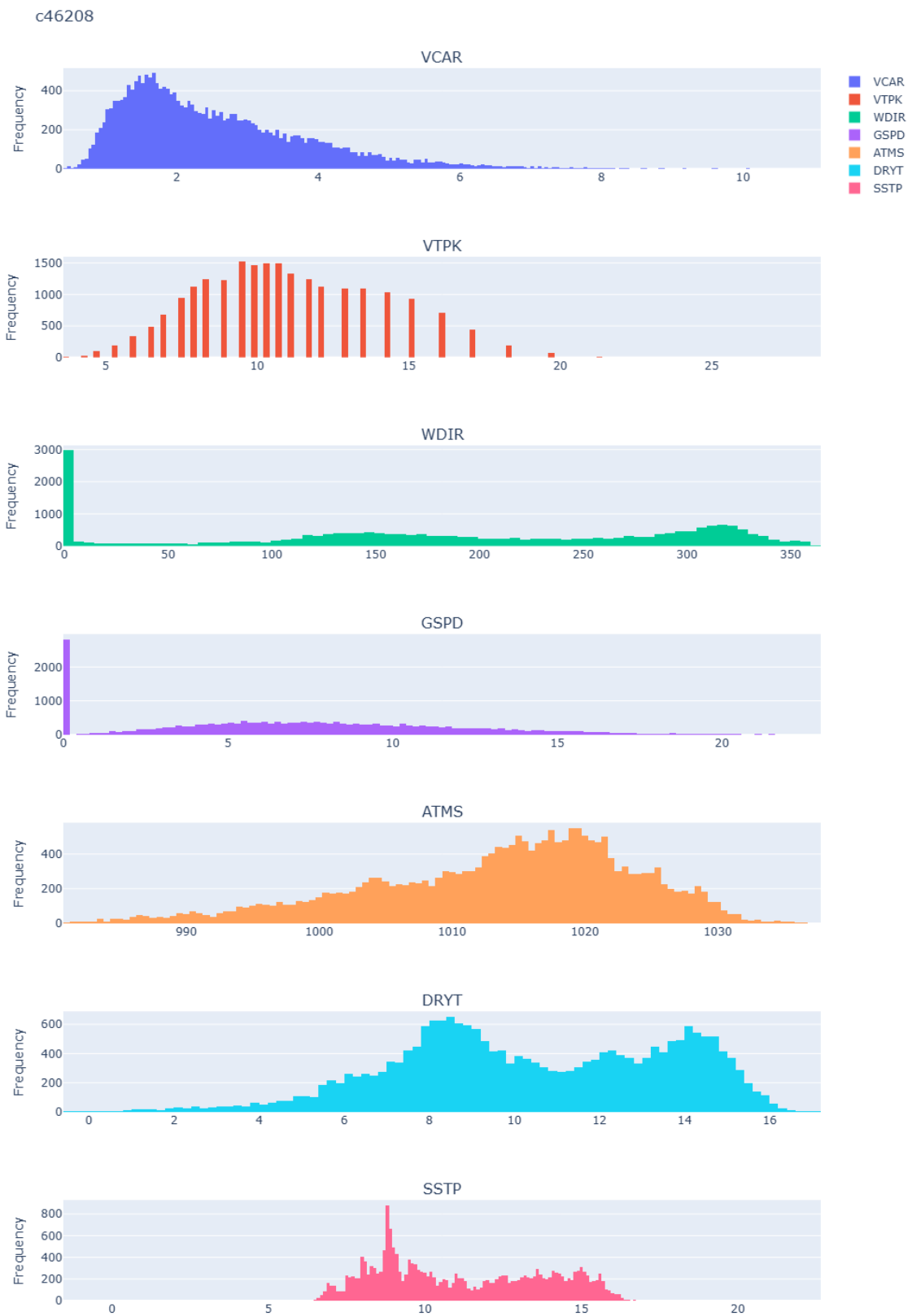


Figure 13: Figures showing the distributions of features or datasets collected from the station c46208. x-axis represents the values, while y-axis denotes the frequency.

- $m$ : The dimension in the Embedding Technique, fixed as  $m = 3$ .
- $p$ : The maximum dimension of persistent homology constructed for the data, taken as  $p \in \{0, 1, 2\}$ .
- $k$ : The first  $k$ -th largest PLs we constructed, taken as  $k = 1$ .
- `optim`: The optimizer used in model training, taken as Adam Optimizer.
- `loss`: The loss function used in training, taken as MSE Loss, defined as:

$$\text{MSE}(\mathbf{y}, \hat{\mathbf{y}}) = \frac{1}{n} \|\mathbf{y} - \hat{\mathbf{y}}\|_2^2. \quad (33)$$

- `batch_size`: The number of training examples used in one iteration. We set it to 50.
- `num_epoch`: The number of complete passes through the training dataset. We set it to 200.
- `act`: The activation function used in the hidden layers, typically taken as ReLU in FNNs and RNNs, sigmoid and tanh in LSTM and GRU.

The workflow is illustrated in Algorithm 1. Initially, we process the original dataset  $\{\mathbf{X}, \mathbf{y}\}$ , applying a best subset selection strategy to identify a subset enriched with information optimally utilizable by the network model `Model`. The training dataset  $\{\mathbf{X}_{\text{train}}^T, \mathbf{y}_{\text{train}}^{T+t'}\}$  comprises daily mean observations of variables specified in section 3.1. The parameter  $t'$ , predefined prior to training, specifies that `Model` is trained to predict observations  $t'$  time units ahead using  $\mathbf{X}_{\text{train}}^T$  as input (see Eq. 5). After determining the hyperparameter combination that yields the highest  $R^2$  score, we fix the hyperparameters that belong to `primary_para_grid`. Subsequently, we generate a new time series of topological features, as illustrated in section 2.7. This new dataset is combined with  $\mathbf{X}_{\text{train}}^T[I_{\text{opt}}]$ , and `Model` is retrained using this combined dataset over the `secondary_para_grid` and with the same `fixed_para_grid`, aiming to optimize the  $R^2$  score.

The dataset is partitioned into 80% for training and 20% for testing. All models are primarily constructed using PyTorch, giotto-tda, and scikit-learn. Training and testing are conducted on a device equipped with a Windows 11 operating system, an Intel Core i9-12900K processor, an NVIDIA RTX 4090 graphics processing unit, and CUDA technology.

---

**Algorithm 1: Working Flow**

---

**Input:**

Original data set:  $\{\mathbf{X}, \mathbf{y}\}$ , where  $\mathbf{X}[i]$  indicates the  $i$ -th features.

Model: a pointer to an instance of a network model.

primary\_para\_grid:  $\{T_{list}, \{\mathbf{X}[i]\}_{i=1}^K\}$ .

secondary\_para\_grid:  $\{lr, num\_layers, hidden\_size, thresh\}$ .

fixed\_para\_grid: hyperparameters that are fixed beforehand.

$\mathbf{X}^{tpo}$ : a tensor with all elements initialized as zeros.

Criterion:  $R^2$  score.

$\{\mathbf{X}_{train}^T, \mathbf{y}_{train}^{T+t'}\}$ : the training data of daily mean of the original data.

**Output:**

Pointers to trained models.

**Initialization;**

**for each subset  $I$  of  $\{\mathbf{X}[i]\}_{i=1}^K$  do**

**for each  $T$  in  $T_{list}$  do**

        Find Model( $\{\mathbf{X}_{train}^T[I], \mathbf{y}_{train}^{T+t'}\}$ ) with the best  $R^2$  score performance over the secondary\_para\_grid with corss validation.

**end**

**end**

**let:**

$T_{opt}$  be the optimum sequence length;

$I_{opt}$  be the optimum subset;

**for each  $\mathbf{X}[i]$  in  $\mathbf{X}[I_{opt}]$  do**

**for each day in the time series  $\mathbf{X}[i]$  do**

**Compute** the point cloud data  $P$  from the hourly observations of the day;

**Compute**  $0 = H_p(\text{VR}_0(P)) \rightarrow \dots \rightarrow \dots \rightarrow H_p(\text{VR}_{\epsilon_n}(P))$ , for  $p \in \{0, 1, 2\}$ ;

**Compute** the persistent diagram  $D = \{b_i, d_i\}$ ;

**Compute**  $\lambda(k, \cdot)$  and  $\bar{\lambda}(k, \cdot)$  for  $k = 1$ ;

$\mathbf{X}^{tpo}[i].append(\bar{\lambda}(k, \cdot))$

**end**

**end**

**set**  $\mathbf{X}_{new} = (\mathbf{X}^{tpo}[I_{opt}], \mathbf{X}[I_{opt}])$ ;

**find:**

Model( $\{\mathbf{X}_{new}^{T_{opt}}, \mathbf{y}_{train}^{T_{opt}+t'}\}$ ) with the best  $R^2$  over the secondary\_para\_grid with corss validation.

**return**

*Two pointers to models, one trained with  $\{\mathbf{X}_{train}^{T_{opt}}[I_{opt}], \mathbf{y}_{train}^{T_{opt}+t'}\}$  and the other with  $\{\mathbf{X}_{new}^{T_{opt}}, \mathbf{y}_{train}^{T_{opt}+t'}\}$ .*

---

### 3.3 Performance metrics

In this section, we present the performance metrics used to evaluate how well the predictions from our models approximate the actual values, indicating the predictive power of the models. Suppose  $\mathbf{y} = \{y_1, y_2, \dots, y_{n-1}, y_n\}$  represents the actual values, while  $\hat{\mathbf{y}} = \{\hat{y}_1, \hat{y}_2, \dots, \hat{y}_{n-1}, \hat{y}_n\}$  are the predictions outputted by our models. The  $R^2$  score is then defined as:

$$R^2(\mathbf{y}, \hat{\mathbf{y}}) = 1 - \frac{\sum_{i=1}^n (y_i - \hat{y}_i)^2}{\sum_{i=1}^n (y_i - \bar{y})^2}, \quad (34)$$

where  $\bar{y} = n^{-1} \sum_{i=1}^n y_i$ . The  $R^2$  score provides a measure of how well the regression predictions approximate the actual data points. Higher  $R^2$  values indicate a better fit. Below is a detailed explanation of the different intervals of  $R^2$  values and their meanings in the context of prediction:

- $0 \leq R^2 < 0.5$ : The model has limited predictive power.
- $0.5 \leq R^2 < 0.7$ : The model has moderate predictive power.
- $0.7 \leq R^2 \leq 1.0$ : The model has high predictive power.

In addition to the  $R^2$  score, we adopted the maximum absolute error (MAE) as another performance metric, defined as follows:

$$\text{MAE}(\mathbf{y}, \hat{\mathbf{y}}) = \|\mathbf{y} - \hat{\mathbf{y}}\|_{\infty}. \quad (35)$$

Another performance metric is the MSE, defined in Eq. 33.

## 3.4 Results

### 3.4.1 FNNs and PHFNNs

In developing FNNs, we set  $t' = 0$  and  $T = 1$ . The feature matrix  $\mathbf{X}$  contains the variables:

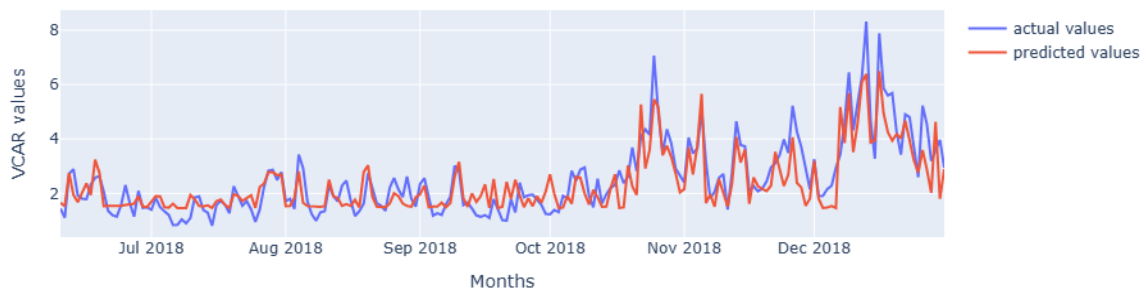
(VTPK, WDIR, GSPD, ATMS, DRYT, SSTP),

while the target vector  $\mathbf{y}$  contains VCAR. In essence, we developed classic regression FNNs that predict the output from the input at the same time step. We present results for two models: FNNs and PHFNNs. The key distinction is that PHFNNs are trained using topological representations extracted from  $\mathbf{X}[I_{\text{opt}}]$ , where  $I_{\text{opt}}$  corresponds to the subset of features with which the FNNs achieved the highest  $R^2$  score.

Table 1: A models comparison between FNNs and PHFNNs. The column 'Search Params' presents the selections of some hyperparameters when the performance metrics on the left columns are obtained.

Station Code	Type	$R^2$ scores	MAE	MSE	Search Params	Features
c46208	FNNs	0.7301	2.158	0.4818	num_layer: 5 lr: $5 \times 10^{-3}$ num_hid: 8 thresh: 0.10	VTPK GSPD ATMS WDIR
	PHFNNs	0.8625	1.887	0.2829	num_layer: 3 lr: $5 \times 10^{-3}$ num_hid: 10 thresh: 0.10	VTPK GSPD ATMS WDIR

FNNs



PHFNNs

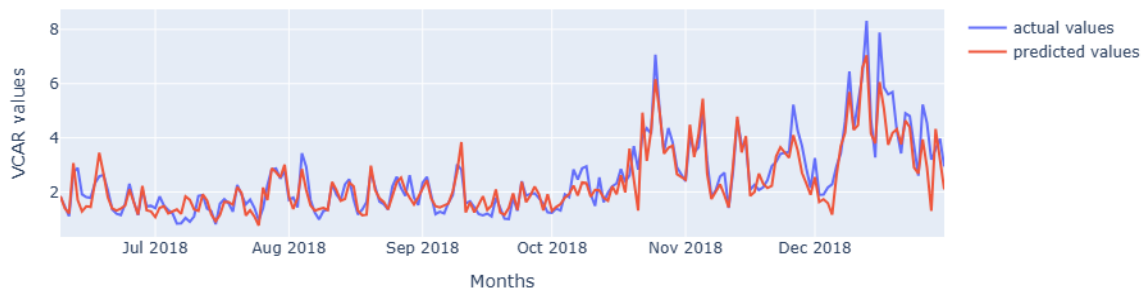


Figure 14: A comparison between FNNs and PHFNNs station c46208, where blue lines represent the actual values and red lines represent the predicted values. (Top) FNNs predicting VCAR values over a 6-months period. (Bottom) PHFNNs predicting VCAR values over the same period.

We present the comparative performance of Feedforward Neural Networks (FNNs) and Polynomial Hybrid Feedforward Neural Networks (PHFNNs) in Table 1, and their approximation to the actual VCAR values in Figure 14. The column labeled ‘Search Params’ lists the hyperparameter values used from `secondary_para_grid` that resulted in the performance metrics shown in the left columns. The ‘Features’ column denotes the optimal feature subset corresponding to these metrics. It is observed that the compared with FNNs, PHFNNs improve the  $R^2$  score by approximately 15%, reduce the maximum absolute error (MAE) by roughly 19%, and decrease the mean squared error (MSE) by about 42%.

### 3.4.2 RNNs and PHRNNs

In the development of RNNs, we fix  $t' = 1$  and treat  $T$  as a hyperparameter. Specifically, we design our models to exploit the sequence  $(\mathbf{X}^{(1)}, \dots, \mathbf{X}^{(T)})$  for predicting future observations one time unit ahead at  $t' = 1$ . Each sequence  $(\mathbf{X}^{(1)}, \dots, \mathbf{X}^{(T)})$  encapsulates the variables:

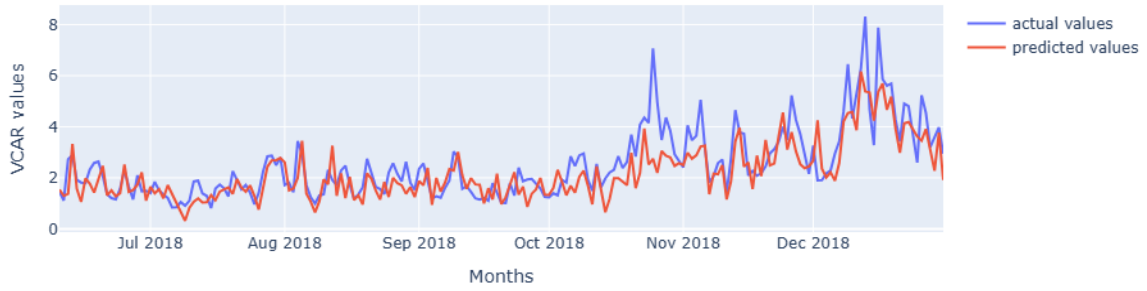
$$(\text{VCAR}, \text{VTPK}, \text{WDIR}, \text{GSPD}, \text{ATMS}, \text{DRYT}, \text{SSTP}),$$

with the target vector  $\mathbf{y}^{(T+t')}$  comprising the variable VCAR. Additionally, we developed two models: RNNs and PHRNNs. The primary difference lies in PHRNNs being trained on topological representations derived from  $\mathbf{X}[I_{\text{opt}}]$  with the sequence length  $T_{\text{opt}}$ , where  $I_{\text{opt}}$  and  $T_{\text{opt}}$  represents the subset of features and the sequence length that yielded the highest  $R^2$  score in the RNNs.

Table 2: A models comparison between RNNs and PHRNNs. The column ‘Search Params’ presents the selections of some hyperparameters when the performance metrics are obtained.

Station Code	Type	$R^2$ scores	MAE	MSE	Search Params	Features
c46208	RNNs	0.6203	4.327	0.6858	num_layer: 2 lr: $5 \times 10^{-3}$ num_hid: 12 thresh: 0.10 $T_{\text{opt}}: 10$	DRYT GSPD ATMS WDIR
	PHRNNs	0.7488	3.693	0.4874	num_layer: 2 lr: $5 \times 10^{-3}$ num_hid: 6 thresh: 0.10 $T_{\text{opt}}: 10$	DRYT GSPD ATMS WDIR

### RNNs



### PHRNNs

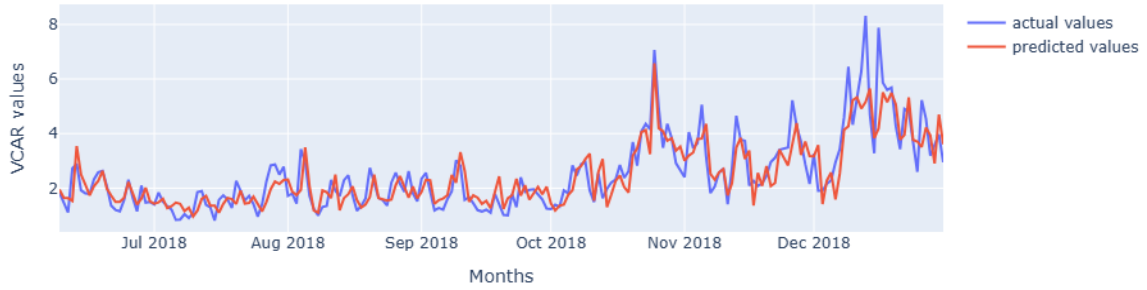


Figure 15: A comparison between RNNs and PHRNNs station c46208, where blue lines represent the actual values and red lines represent the predicted values. (Top) RNNs predicting VCAR values over a 6-months period. (Bottom) PHRNNs predicting VCAR values over the same period.

We presented the results and comparison in Table 2 and Fig.15. Compared with RNNs, PHRNNs improve the  $R^2$  score by approximately 20%, reduce MAE by roughly 16%, and decrease MSE by about 30%.

### 3.4.3 LSTM and PHLSTM

The development of LSTM and PHLSTM follows a similar methodology to that of RNNs and PHRNNs. We have presented the results and comparisons in Table 3 and Figure 16. Compared with RNNs, PHRNNs enhance the  $R^2$  score by approximately 23%, reduce the MAE by about 1.30, and decrease the MSE by roughly 34%. However, achieving these improvements requires an optimal sequence length of 39%, which is more demanding than the requirements for RNNs and PHRNNs.

Table 3: A models comparison. The column 'Search Params' presents the selections of some hyperparameters when the performance metrics are obtained.

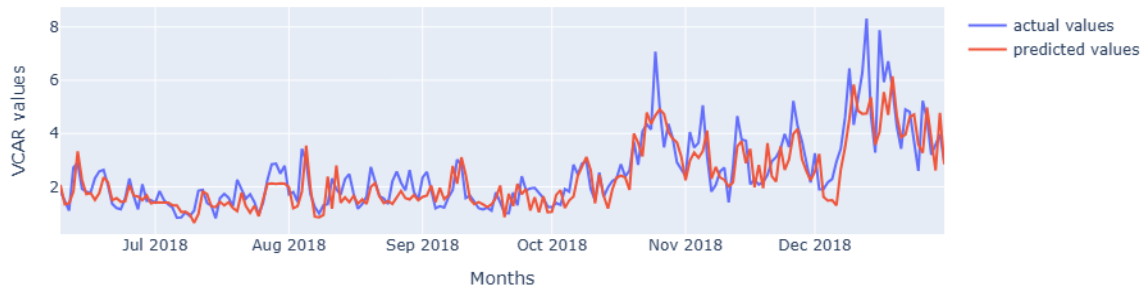
Station Code	Type	$R^2$ scores	MAE	MSE	Search Params	Features
<b>c46208</b>	LSTM	0.6493	3.818	0.5864	num_layer: 2 lr: $5 \times 10^{-3}$ num_hid: 10 thresh: 0.10 T: 30	VTPK GSPD WDIR
	PHLSTM	0.7904	2.507	0.3593	num_layer: 6 lr: $5 \times 10^{-3}$ num_hid: 18 thresh: 0.10 T: 30	VTPK GSPD WDIR

Table 4: A models comparison. The column 'Search Params' presents the selections of some hyperparameters when the performance metrics are obtained.

Station Code	Type	$R^2$ scores	MAE	MSE	Search Params	Features
<b>c46208</b>	GRU	0.6224	4.083	0.6023	num_layer: 2 lr: $5 \times 10^{-3}$ num_hid: 34 thresh: 0.10 T: 20	VTPK GSPD WDIR ATMS
	PHGRU	0.7884	2.628	0.3814	num_layer: 4 lr: $5 \times 10^{-3}$ num_hid: 12 thresh: 0.10 T: 20	VTPK GSPD WDIR ATMS



### LSTM



### PHLSTM

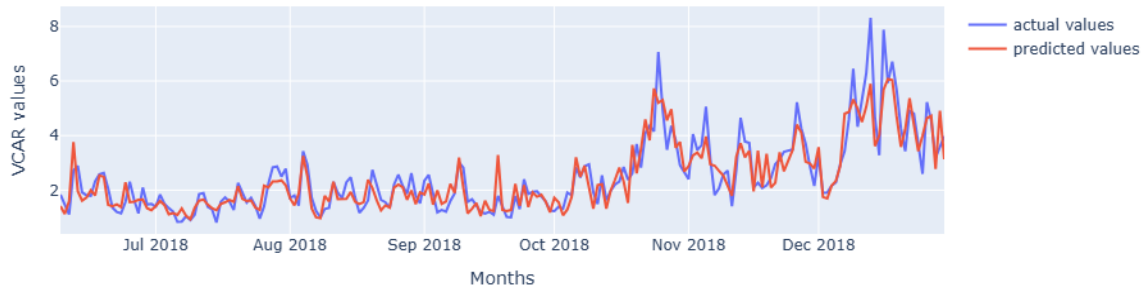


Figure 16: A comparison between LSTM and PHLSTM station c46208, where blue lines represent the actual values and red lines represent the predicted values. (Top) LSTM predicting VCAR values over a 6-months period. (Bottom) PHLSTM predicting VCAR values over the same period.

### 3.4.4 GRU

The last model is RNNs with GRU, the working flow is similar to those of other variants of RNNs. We show the results in Table.4 and Fig.17. The sequence length is less demanding than LSTM, however, the performance is slightly worse. Compared with GRU, PHGRU enhances the  $R^2$  score by approximately 25%, reduce the MAE by about 35%, and decrease the MSE by roughly 36%.

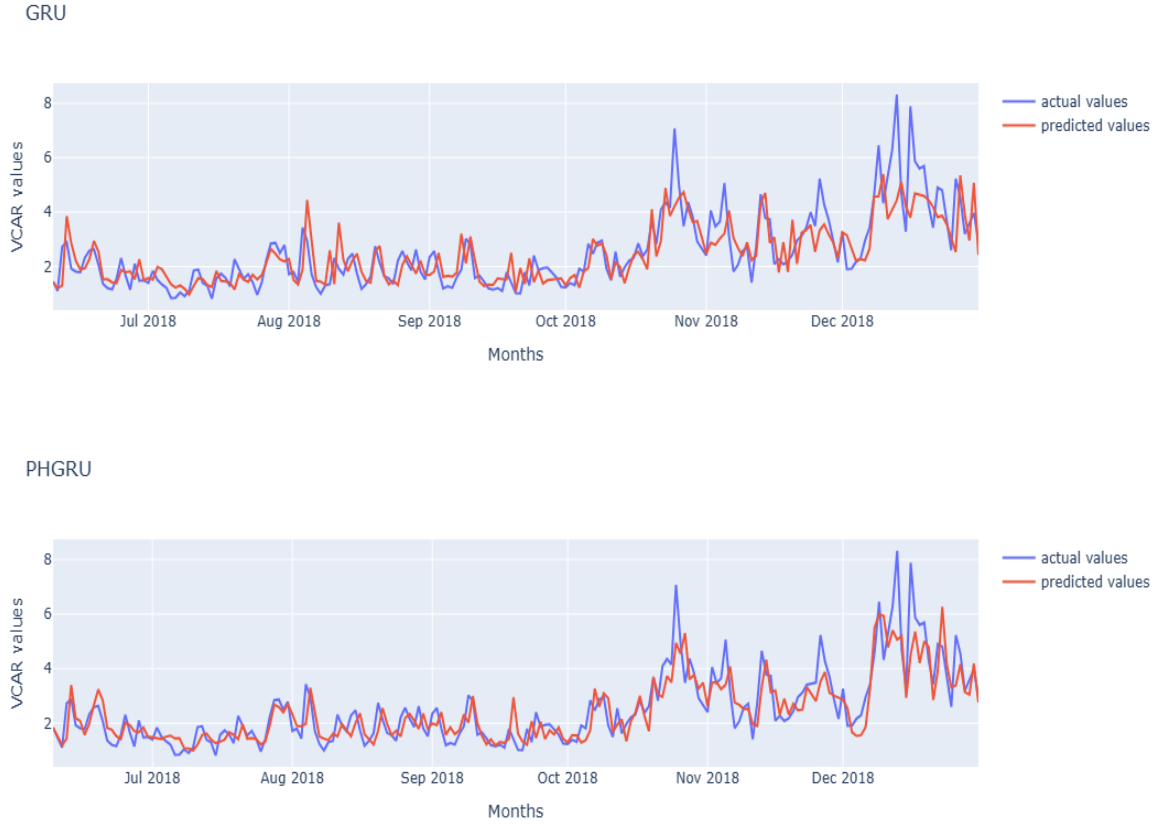


Figure 17: A comparison between LSTM and PHLSTM station c46208, where blue lines represent the actual values and red lines represent the predicted values. (Top) LSTM predicting VCAR values over a 6-months period. (Bottom) PHLSTM predicting VCAR values over the same period.

## 4 Discussions

### 4.1 Contributions

Our proposed models contribute to the study and prediction of time-series data. The improvement of PH neural network models over standard models is consistent. Here, consistent means that the improvement can be achieved even with different selections of features and model architecture designs.

First, the enhancement in generalization performance is consistently observed, irrespective of the number of features selected. To show this, we randomly selected  $i$  features at each step, where  $1 \leq i \leq 6$ . At each step, we trained a FNN model using the randomly selected features and a PHFNN model incorporating the topological features derived from these selected features. Both models maintained a consistent architecture across the steps, characterized by `num_layers = 2` and `hid_size = 12`. The generalization performance of both models, measured by the  $R^2$  score, is depicted in Fig.18. The results clearly demonstrate that, regardless

of the number of features utilized, the PHFNs consistently outperformed the FNNs in terms of generalization performance. This experiment, alongside the findings presented in Section 3, underscores the efficacy of employing feature engineering techniques via persistent homology and persistent landscape to enhance the predictive capabilities of artificial neural network models in time-series prediction.

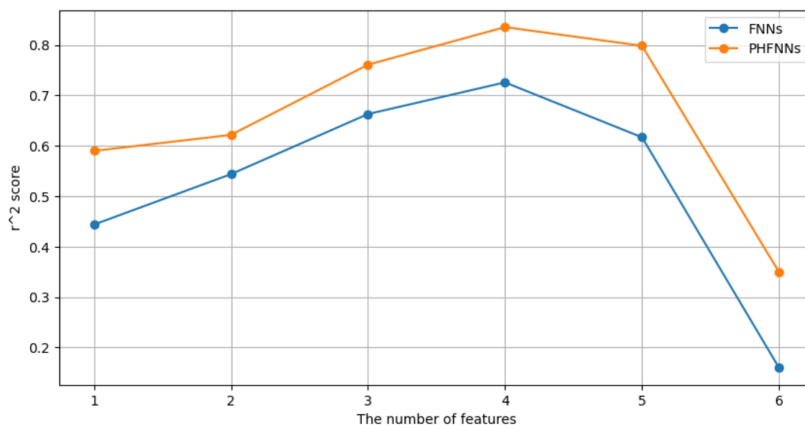


Figure 18: The  $R^2$  scores of FNNs and PHFNs on testing data set.  $x$ -axis represents the number of features randomly selected at each step, while  $y$ -axis represents the  $R^2$  score.

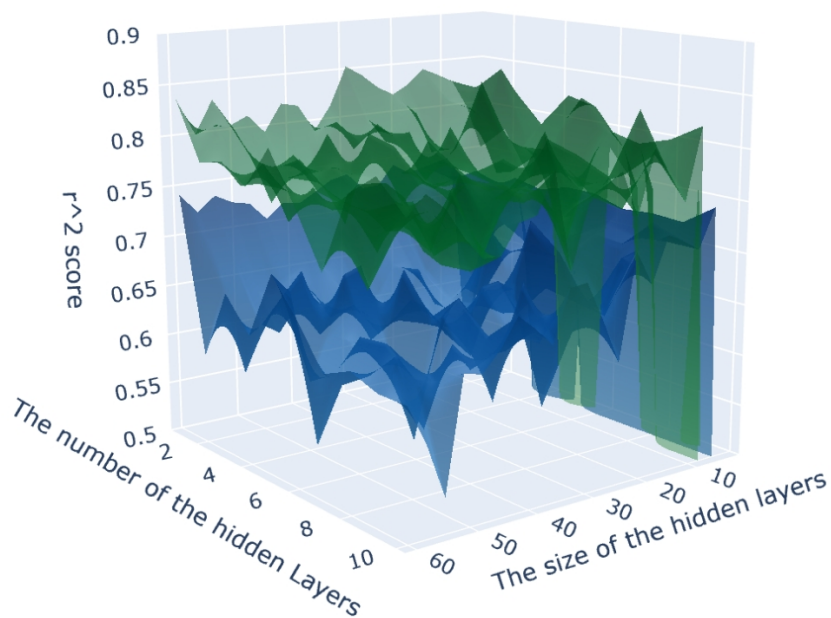


Figure 19: The  $R^2$  scores of FNNs and PHFNs on the testing dataset. The green surface represents the results from PHFNs, while the blue surface represents those from FNNs. The bottom plane displays the grid of hidden layer numbers and sizes.

Second, the enhancement of engineering topological features aligns with the structures of

the models. To demonstrate this, we fixed the features as (VTPK, WDIR, GSPD, ATMS), where FNNs achieved the highest  $R^2$  score, and varied the number of hidden layers across

$$\{i \mid 1 \leq i \leq 10\}$$

and the size of each hidden layer across

$$\{i \times 3 \mid 1 \leq i \leq 20\}.$$

The results are plotted in Fig.19. In this figure, except for a few points indicating extreme underfitting (possibly due to incorrect random initialization or the small size of hidden layers), PHFNN models consistently achieved better predictive power in terms of  $R^2$  score compared to FNN models. This comparison is undoubtedly somewhat unfair to PHFNN models, as we compared them on the feature subset over which FNNs achieved the highest  $R^2$  score. However, even on this subset, PHFNNs outperform FNNs.

Our work contributes to the study of oceanographic data, specifically the wave height in several ways:

- Predicting wave height is essential for the safety of all types of vessels at sea—from small fishing boats to large cargo ships. Accurate wave forecasts help mariners avoid hazardous conditions, plan safer routes, and reduce the risk of capsizing or accidents.
- Understanding and predicting wave heights is crucial for coastal planning and infrastructure development. It helps in designing suitable coastal defenses, like seawalls and breakwaters, to protect against erosion and flooding. Accurate predictions are also important for managing and mitigating the impacts of storm surges and tsunamis.
- Studying historical wave height data contributes to climate research, helping scientists understand changes in storm patterns, sea levels, and overall marine dynamics under different climate scenarios.

## 4.2 Limitations

- The initialization of states and hidden layers in FNNs, RNNs, LSTM, and GRU models with a normal distribution  $\mathcal{N}(0, 1)$ , coupled with random starting points for the gradient descent method, may lead to extreme underfitting and unstable learning.
- The scope of the neural network structures explored in our search for the highest  $R^2$  score was not extensive. The range of layers—critical in terms of computational resources—was from 2 to 40, and the range of sizes was from 3 to 60. This limited grid size might cause us to miss other combinations where models could perform better.

- The back-propagation step occasionally got stuck and failed to steadily decrease the loss function as training progressed, necessitating additional training epochs or a restart of the training process.
- We extracted only one topological feature of  $H_0$ ,  $H_1$ , and  $H_2$  from a single data feature each day, yet there are compelling reasons and many possibilities to explore a broader range of topological features, such as standard deviation, maximum lifetime, or distances between persistent diagrams.
- In this work, we employed standard variants of FNNs, RNNs, LSTM, and GRU. However, other models exist that might better suit wave height data. For instance, the Adaptive Neuro-Fuzzy Inference System can effectively predict wave heights as a classic regressor without producing time-ahead outputs.

## 5 Conclusions

In this comprehensive study, we focused on enhancing the predictive capabilities of neural network models for time-series analysis, particularly in the context of wave height prediction—an essential task with significant implications in maritime safety, climate monitoring, and coastal management. The primary innovation of our research lies in the integration of computational topology to improve the feature engineering process, thereby refining the input data for better model performance.

By employing advanced computational topology techniques, we systematically extracted novel topological features from the time-series data. These features, which capture intricate data structures that traditional methods might overlook, have proven to be exceptionally beneficial in boosting the predictive accuracy of our neural network models.

Throughout our experiments, we utilized a range of neural network architectures, including FNNs, RNNs, LSTM, and RNNs equipped with GRU. Our results have been promising, demonstrating a tangible improvement in the models' performance metrics.

Specifically, the inclusion of topological features led to an increase in the  $R^2$  score of approximately 15% for FNNs when applied in a regression context. For models designed for time-ahead predictions, the performance gains were even more pronounced, with improvements of 20%, 23%, and 25% in the  $R^2$  scores for RNNs, LSTM, and GRU models, respectively. Alongside these improvements in predictive accuracy, our models also exhibited significant reductions in both maximum errors and mean squared errors, further underscoring the efficacy of our approach.

These enhancements are not just numerical but translate into more reliable and robust models that can be effectively used in practical settings where accurate wave height prediction is critical. This research not only contributes to the existing body of knowledge but also opens

new avenues for future studies to explore other complex time-series forecasting problems using topological data analysis.

## Conflict of Interest

The authors declare that they have no conflicts of interest relevant to the content of this article.

## Ethics Approval

This study did not involve any human participants, animal subjects, or data collected from social media platforms that require ethical approval.

## Funding

This research did not receive any specific grant from funding agencies in the public, commercial, or not-for-profit sectors.

## Data Availability

The data that support the findings of this study are available from the corresponding author upon reasonable request.

## References

- [1] H. Cheng, P.-N. Tan, J. Gao, and J. Scripps, “Multistep-ahead time series prediction,” in *Advances in Knowledge Discovery and Data Mining: 10th Pacific-Asia Conference, PAKDD 2006, Singapore, April 9-12, 2006. Proceedings 10*. Springer, 2006, pp. 765–774.
- [2] Z. Han, J. Zhao, H. Leung, K. F. Ma, and W. Wang, “A review of deep learning models for time series prediction,” *IEEE Sensors Journal*, vol. 21, no. 6, pp. 7833–7848, 2019.
- [3] S. F. Crone and N. Kourentzes, “Feature selection for time series prediction—a combined filter and wrapper approach for neural networks,” *Neurocomputing*, vol. 73, no. 10-12, pp. 1923–1936, 2010.
- [4] R. Turkes, G. F. Montufar, and N. Otter, “On the effectiveness of persistent homology,” *Advances in Neural Information Processing Systems*, vol. 35, pp. 35 432–35 448, 2022.

- [5] H. J. Van Veen, N. Saul, D. Eargle, and S. W. Mangham, “Kepler mapper: A flexible python implementation of the mapper algorithm.” *Journal of Open Source Software*, vol. 4, no. 42, p. 1315, 2019.
- [6] M. Köppen, “The curse of dimensionality,” in *5th online world conference on soft computing in industrial applications (WSC5)*, vol. 1, 2000, pp. 4–8.
- [7] T. K. Dey and Y. Wang, *Computational topology for data analysis*. Cambridge University Press, 2022.
- [8] Y. Skaf and R. Laubenbacher, “Topological data analysis in biomedicine: A review,” *Journal of Biomedical Informatics*, vol. 130, p. 104082, 2022.
- [9] I. Obayashi, T. Nakamura, and Y. Hiraoka, “Persistent homology analysis for materials research and persistent homology software: Homcloud,” *journal of the physical society of japan*, vol. 91, no. 9, p. 091013, 2022.
- [10] N. F. S. Zulkepli, M. S. M. Noorani, F. A. Razak, M. Ismail, and M. A. Alias, “Hybridization of hierarchical clustering with persistent homology in assessing haze episodes between air quality monitoring stations,” *Journal of environmental management*, vol. 306, p. 114434, 2022.
- [11] Y. Reani and O. Bobrowski, “Cycle registration in persistent homology with applications in topological bootstrap,” *IEEE Transactions on Pattern Analysis and Machine Intelligence*, vol. 45, no. 5, pp. 5579–5593, 2022.
- [12] E. Munch, “Applications of persistent homology to time varying systems,” Ph.D. dissertation, Duke University, 2013.
- [13] C. S. Pun, K. Xia, and S. X. Lee, “Persistent-homology-based machine learning and its applications—a survey,” *arXiv preprint arXiv:1811.00252*, 2018.
- [14] J. Townsend, C. P. Micucci, J. H. Hymel, V. Maroulas, and K. D. Vogiatzis, “Representation of molecular structures with persistent homology for machine learning applications in chemistry,” *Nature communications*, vol. 11, no. 1, p. 3230, 2020.
- [15] M. Talaat, M. Farahat, N. Mansour, and A. Hatata, “Load forecasting based on grasshopper optimization and a multilayer feed-forward neural network using regressive approach,” *Energy*, vol. 196, p. 117087, 2020.
- [16] B. Amiri-Ramsheh, R. Zabihi, and A. Hemmati-Sarapardeh, “Modeling wax deposition of crude oils using cascade forward and generalized regression neural networks: Application to crude oil production,” *Geoenergy Science and Engineering*, vol. 224, p. 211613, 2023.

- [17] F. Stulp and O. Sigaud, “Many regression algorithms, one unified model: A review,” *Neural Networks*, vol. 69, pp. 60–79, 2015.
- [18] B. E. Scarfe, T. R. Healy, and H. G. Rennie, “based surfing literature for coastal management and the science of surfing—a review,” *Journal of Coastal Research*, vol. 25, no. 3, pp. 539–557, 2009.
- [19] C. Izaguirre, F. J. Méndez, M. Menéndez, and I. J. Losada, “Global extreme wave height variability based on satellite data,” *Geophysical Research Letters*, vol. 38, no. 10, 2011.
- [20] P. V. de Campos Souza, “Fuzzy neural networks and neuro-fuzzy networks: A review the main techniques and applications used in the literature,” *Applied soft computing*, vol. 92, p. 106275, 2020.
- [21] R. M. Schmidt, “Recurrent neural networks (rnns): A gentle introduction and overview,” *arXiv preprint arXiv:1912.05911*, 2019.
- [22] R. C. Staudemeyer and E. R. Morris, “Understanding lstm—a tutorial into long short-term memory recurrent neural networks,” *arXiv preprint arXiv:1909.09586*, 2019.
- [23] S. Nosouhian, F. Nosouhian, and A. K. Khoshouei, “A review of recurrent neural network architecture for sequence learning: Comparison between lstm and gru,” 2021.
- [24] N. Otter, M. A. Porter, U. Tillmann, P. Grindrod, and H. A. Harrington, “A roadmap for the computation of persistent homology,” *EPJ Data Science*, vol. 6, pp. 1–38, 2017.